PRODUCTION PROCESS

Evaluation and optimisation of a slurry-based layer casting process in additive manufacturing using multiphase simulations and spatial reconstruction

P. Erhard[1] · A. Seidel[2] · J. Vogt[3] · W. Volk[1,2] · D. Günther[1]

Abstract

Slurry-based 3D printing allows ceramic green bodies to be fabricated at high packing densities. In contrast to powder-based binder jetting, full densification of printed parts can be achieved in a subsequent sintering step as fine particles dispersed in a suspension are cast and compacted. Slurry-based 3D printing is thus expected to overcome the application limits of the powder-based alternative in metal casting in terms of unfavorable properties like high surface roughness, low density and low mechanical strength. To ensure stress-free drying and therefore high qualities of the compounds made in layers, it is crucial to fabricate single layers with a high level of homogeneity. This paper presents a CFD model based on the open-source simulation environment *OpenFOAM* to predict the resulting homogeneity of a cast slurry layer with defined parameter sets or coater geometries using the Volume-Of-Fluid method. Moreover, a novel method of spatial reconstruction is proposed to evaluate the surface quality of layers on a minimised computional demand. By comparing the results of the simulation with the real macroscopic behaviour determined in experiments, the approach is found to be a useful tool for suggesting suitable parameters and coater geometries for processing slurries. A precise reconstruction of the outline of the coating area with different process parameters and an approximate prediction of the effect on surface roughness was achieved.

1 Introduction

Products processed by additive manufacturing (AM) technologies are gaining more and more attention in industrial applications as near net shape components can be produced to a high level of complexity [1, 23]. The 3D printing (3DP) method was developed at the Massachusetts Institute of Technology (MIT) and initially filed as a patent by Sachs et al. in 1989 [18]. It comprises the repeated process steps of spreading a layer of particle material, applying a binder medium to locally bond the particles in each layer and lowering the building platform. The good scalability of printing speeds and sizes is a key feature of 3DP technology compared to other AM methods and has been a crucial point for successfully establishing the binder jetting of sand moulds and cores in the casting industry [5, 24].

However, the application limits of binder-jetted moulds and cores will be extended through the promising technique called "slurry-based 3D Printing" (S-3DP) that is investigated in this study. Figure 1 shows a diagram of the investigated process. An inkjet printhead applies binder to pre-densified layers produced from slurry material to define the part contour [19].

Powder-based 3D printing (P-3DP) technologies exhibit relatively low powder bed densities. Depending on themethod of application, powder size distribution, morphology and process parameters, the powder packing densities may be less than 35 % [17] or even as low as 25 % [29] of the theoretical density [bulk density/ particle density]. Mostafai et al. [11] review various novel approaches for increasing green densities to a theoretical density of 50 % or more using different binder jetting materials and methods, highlighting

✉ P. Erhard
   patricia.erhard@igcv.fraunhofer.de

1 Fraunhofer IGCV, Garching, Germany

2 Technical University of Munich, Garching, Germany

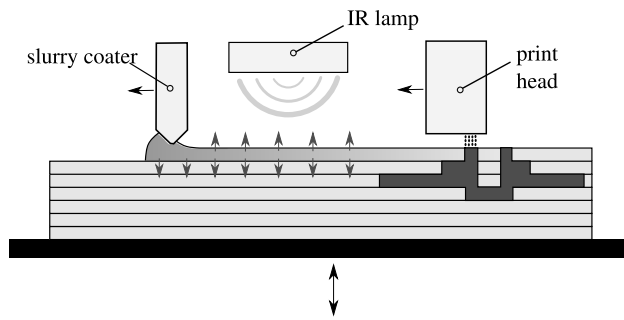3 Fraunhofer ISC/ Center for High-Temperature Materials and Design, Bayreuth, Germany

Fig. 1 Diagram of the slurry-based 3D printing process

the need for high-density parts in different industries. Zocca et al. [30] found that increased powder packing densities of >55 % theoretical density are possible with S-3DP. This leads to an increase of inter-particle contacts, which promotes densification during sintering, potentially enabling full part densification.

The formation of ceramic layer compounds combines characteristics of tape casting and slip casting [13]. It has been studied in different setups and investigated for Selective Laser Sintering [12, 22] or the 3DP method [30]. Excess material can be used to run the process without a precise control of the feed material [13]. Little work has been carried out explicitly on premetered slurry coating devices for additive manufacturing [28]. However, investigations have been conducted into coating methods [8] and coater designs for suspensions [9] in related disciplines.

Yen [28] designed a novel coater geometry, including a coat hanger distribution chamber based on both slot-die coating and tape casting, and studied the influence of geometrical parameters of the coater geometry and of process parameters such as the preloading time. It is suggested that the preloading time (the time slurry is deposited in front of the coater before it starts moving) prevents the so called sawtooth effect. This defect is due to the slurry being extruded as beads before building up a slurry front. Yen [28] reported the benefit of uniform water permeation resulting from a simultaneous slurry feed during movement. The slurry was extruded with a feed rate matched to the casting speed and with low amounts of residual slurry.

Since the authors are not aware of any publications dealing with the numerical simulation of the S-3DP process itself, this elaboration builds upon recognitions from the related discipline of tape casting. Loest et al. [10] carried out two-dimensional simulations and modelled ceramic slurry as a Bingham-Plastic, i.e. a homogeneous mixture of a liquid and particles. The focus was on minimising recirculation inside the coater.

Wonisch et al. [27] simulated the macroscopic flow in the entire three-dimensional domain as well as the orientation of the dispersed particles. Their simulation included a two-step
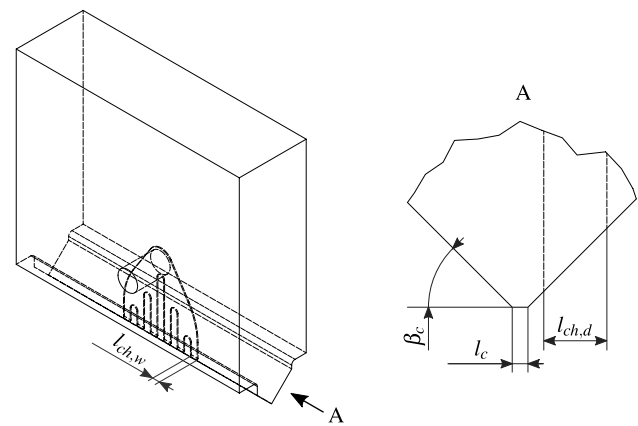

Fig. 2 Geometry of the waterfall coater

process consisting of a Smoothed Particle Hydrodynamics (SPH) simulation and a subsequent solution of Jeffery's equation for the ellipsoidal particles. The three phases liquid, particles and air were simulated independently.

Jabbari et al. [7] evaluated different interface methods when simulating a multiphase flow of non-Newtonian ceramic slurries in tape casting. They state that any one of three equations - Bingham, Herschel–Bulkley or Ostwald-de-Waele power law constitutive equations - could be used to model non-Newtonian fluids (like ceramic slurries).

The objective of this paper is to propose a CFD approach to simulate the slurry deposition process, to suggest appropriate process parameters and advanced coater geometries for homogeneous layers, and thus to create the basis for faster process developments in S-3DP.

2 System description

A quartz slurry formulation for fabricating thin-walled casting cores was developed prior to this study [25]. Moreover, a coater geometry suitable for processing the developed slurry has been designed and investigated in an experimental study [21]. The starting point of this study was the previously eleborated physical setup of the coating unit, hereafter referred to as "waterfall coater" (Fig. 2). It has been designed as a scalable geometry for a precise slurry application to substrates. The relevant geometrical parameters of the coater are shown in Table 1. The waterfall coater geometry contains six channels of 3 mm width and 0.4 mm depth with gaps of 3 mm between the channels.

Yen [28] reported the formation of beads in the coat hanger design used in his studies and suggested a preload phase of slurry deposition to transform the beads into a single slurry front. The waterfall coater shows a targeted homogeneous bead formation before building up a slurry front.

Table 1 Geometric parameters of the waterfall coater

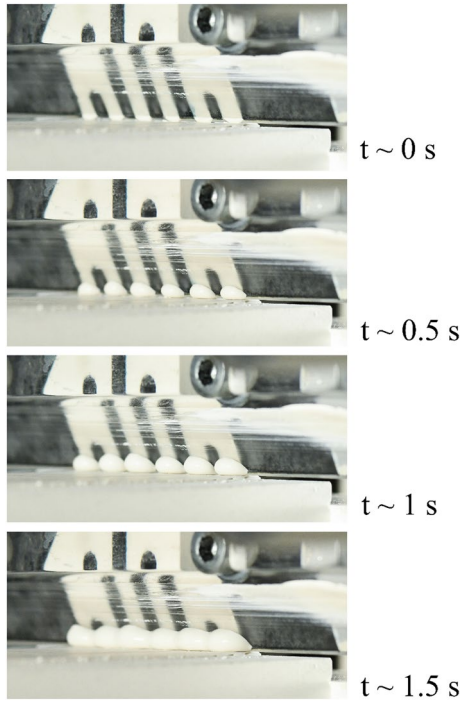| Geometric parameter	Variable	Value	Unit
Channel width	$l_{ch,w}$	3	mm
Channel depth	$l_{ch,d}$	0.4	mm
Chamfer distance	l_c	0.1	mm
Chamfer angle	β_c	45	°

Fig. 3 Phases of slurry outflow during preloading. A continuous slurry front is formed upon the single beads flowing from six channels within the preloading time $t_{preload} = 1.5$ s at a slurry pressure $p_{slurry} = 0.95$ bar. Photos taken by manual triggering

Figure 3 displays the phases of the slurry outflow during the preloading phase with the investigated coater geometry.

The process to be modelled herein comprises the following steps: first, the outflow of slurry during the preloading phase (without movement of the coater/ substrate) is observed. Second, the layer casting itself is modelled by describing a movement of the substrate parallel to the slurry outflow, which can be devided into a phase of linear acceleration and a phase of constant velocity.

3 Modelling and simulation setup

The simulation method presented in this article uses the CFD approach to model the behaviour of the two apparent phases (air and slurry) as well as their interface in three dimensions. The numerical solver *interFoam* from the open-source
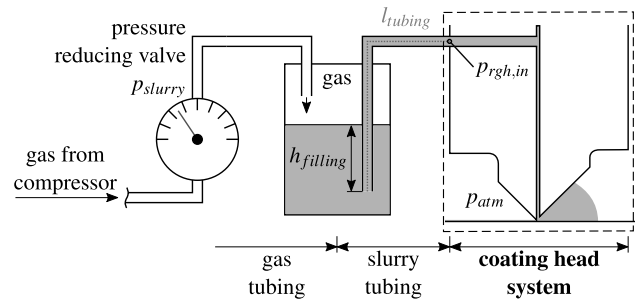

Fig. 4 Pressure levels in the coating system and division into sub-domains. The sub-domain this study deals with is highlighted

Table 2 Result of the pre-processing sub-simulation. $\bar{p}_{rgh,in}$ is set as a boundary condition in the coating simulations

p_{slurry} in Pa	$h_{filling}$ in mm	$\bar{p}_{rgh,in}$ in Pa
9.5×10^4	70	3.1732×10^4

simulation software *OpenFOAM* is used for this purpose in the version *v1912* [16].

3.1 Definition of the simulation domain

As shown in Fig. 4, the simulation domain is seperated into sub-domains to decrease the computional demand. The coating head system itself distributes the slurry to form layers and is fed with slurry from a reservoir via a slurry tubing (600 mm in length, inner diameter 4 mm).

The simulations performed herein are made up of two connected transient sub-simulations. The first step calculates the pressure drop along the slurry tubing. This pre-processing sub-simulation examines the fluid flow from the slurry reservoir to the inlet of the coating head using a coarse mesh and results in an area-integrated pressure $\bar{p}_{rgh,in}$ that is used in the subsequent sub-simulation as a fixed boundary condition at the inlet. The simulation can be split into two sub-simulations since preliminary investigations showed that $\bar{p}_{rgh,in}$ becomes quasi-stationary and pressure changes at the inlet during the coating process itself are negligible. This article will focus on the simulation of the actual coating process and will not discuss the pre-processing step.

3.2 Boundary conditions and discretisation

The area-averaged pressure $\bar{p}_{rgh,in}$, the result of the pre-processing simulation, is set as a boundary condition. It is calculated for the pre-set conditions displayed in Table 2, being a pressure set on the pressure reducing valve of

$p_{slurry} = 0.95$ bar and a filling height of $h_{filling} = 70$ mm in the reservoir.

The corresponding simulation domain with its boundaries is depicted in Figs. 5 and 6 for a gap height of $h_g = 0.1$ mm. A refined mesh is used to represent the coating head geometry as well as its surroundings, including the underlying substrate. The mesh consists of 172710 hexahedral and split-hexahedral cells. An atmospheric condition ($p_{atm} = 0$ Pa) is prescribed at the atmosphere patches. The substrate and the cavity wall patches are treated as impermeable surfaces (*noSlip* condition). The coating head is pre-filled up to its outlet. The coater movement is modelled by inscribing a velocity at the substrate patch. The simulated time is set to $t_s = 2.5$ s.

3.3 CFD methods

The *interFoam* solver uses the Volume-Of-Fluid (VOF) method in combination with the Continuum-Surface-Force (CSF) method to capture the interface between two immiscible fluids [16]. This leads to an extension of the conventional Navier-Stokes and continuity equation used in CFD by an additional convection term for the volume fraction of the first phase α. The VOF method and the corresponding CSF method for modelling multiphase flows have already been described in literature, e.g. Nieves-Remacha et al. [15] and Brackbill [2]. As a ceramic slurry phase usually shows non-Newtonian, respectively shear-thinning, behaviour [4, 14], a power-law rheology model is used to account for this behaviour. The air phase is modelled as a Newtonian fluid.
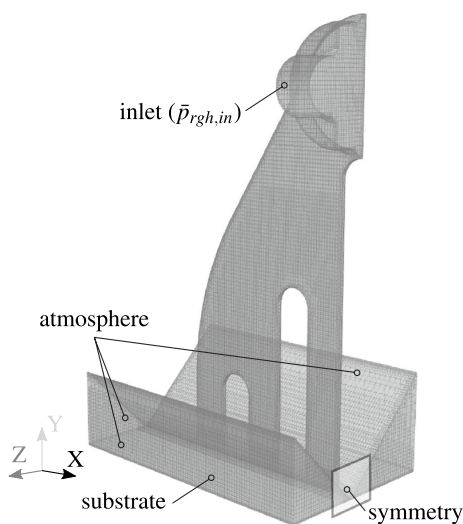

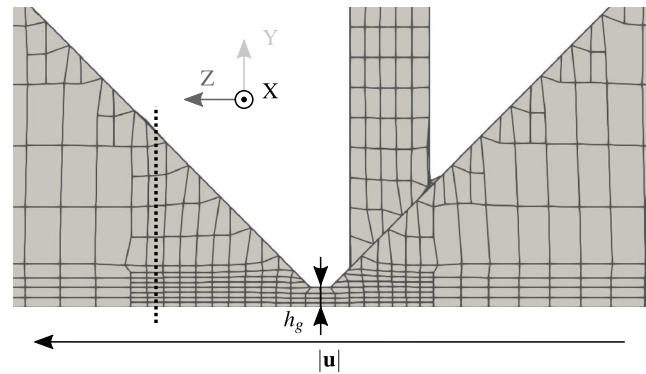**Fig. 5** Simulation domain for the coating process

Fig. 6 Detail of the simulation domain in the near-gap region for $h_g = 0.1$ mm. The evaluation plane for the spatial reconstruction is highlighted with a dotted line

3.4 Rheology model

To characterise the fluid behaviour of the selected slurry material, rheology measurements have been conducted prior to this study as described in [25]. The results from the experimental viscosity measurements are incorporated in a non-Newtonian power law rheology model to treat the slurry phase in the transient simulations. The definition of the power law model in *OpenFOAM* follows as [16]:

$$\nu = k\,\dot{\gamma}^{n-1}, \text{ with } \nu_{min} \leq \nu \leq \nu_{max}. \tag{1}$$

Here, ν is the kinematic viscosity, ν_{min} is the lower viscosity limit, ν_{max} is the upper viscosity limit, $\dot{\gamma}$ is the strain rate and k and n are model parameters. The *Q24* slurry shows a different viscosity for increasing strain rates $\dot{\gamma}$ compared to decreasing strain rates. Both the increasing and the decreasing strain rate hysteresis part is incorporated into the rheology model by calculating the mean of the two halves. The power law model parameters k and n are fitted to the resulting data using a non-linear Levenberg–Marquardt least-squares approach. The Root Mean Square Error RMSE of the model fit is 9.81×10^{-4} m$^2 \cdot$ s^{-1}. ν_{min} and ν_{max} are set to the maximal and minimal ν occurring in the experimental data. The resulting parameters are summarised in Table 3.

The density of the slurry is calculated by its composition and is $\rho_s = 1725.4$ kg $\cdot$ m^{-3}. The properties of air are adapted and simplified from [26]. They result in $\rho_a = 1$ kg $\cdot$ m^{-3} and $\nu_a = 1.48 \times 10^{-5}$ m$^2 \cdot$ s^{-1}. The surface tension is assumed to

Table 3 Rheology parameters of the power law model for the *Q24* slurry

k in m$^2 \cdot$ s^{-1}	n in −	ν_{min} in m$^2 \cdot$ s^{-1}	ν_{max} in m$^2 \cdot$ s^{-1}
1.228×10^{-2}	3.794×10^{-1}	1.772×10^{-4}	2.139×10^{-1}

be dominated by the carrier liquid of the slurry (de-ionised water) and is adequately set to $\sigma_{s,a} = 7 \times 10^{-2}\,\mathrm{N \cdot m^{-1}}$ [26].

3.5 Spatial reconstruction

As the investigated process of applying slurry to a substrate is of dynamic nature, a method for a global evaluation of the slurry layer quality in the entire building area that requires little computing times is of major interest for additive manufacturing technologies. The transient coating simulation calls for a higher mesh resolution in the region of interest to model the slurry behaviour to a satisfactory level. The slurry layer length is of magnitude 10^2 bigger than the gap height in the current prototype state and is likely to increase even further on an industrial scale. Generating a sufficient mesh over the entire length of the slurry layer would require uneconomic simulation resources. The spatial reconstruction method shown in Fig. 7 is proposed to allow an evaluation of the entire slurry layer whilst keeping the computational effort little.

Ceramic slurry typically shows a shear-thinning behaviour. As a consequence, its kinematic viscosity ν is high for strain rates $\dot{\gamma}$ approaching 0. During the deposition process, the slurry height decreases after the slurry passes the coating gap. The slurry forms a downstream meniscus and then

remains within a small range (Fig. 8). Once in this state, the slurry height is mainly influenced by gravitational force. Neglecting this influence, the slurry layer retains its shape throughout the entire coating process.

A stationary evaluation plane is determined perpendicular to the coating direction within the region of a sufficient
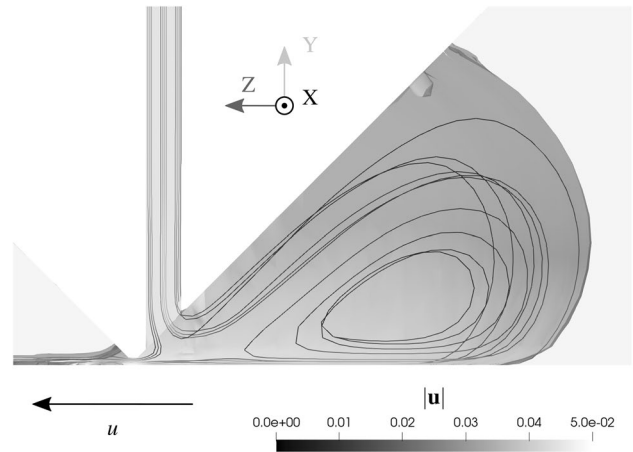

Fig. 8 Exemplary simulation results for simulation No. 1 at $t = 2.25\,\mathrm{s}$. The isosurface for $\alpha = 0.5$ and the stream lines within the slurry phase are shown
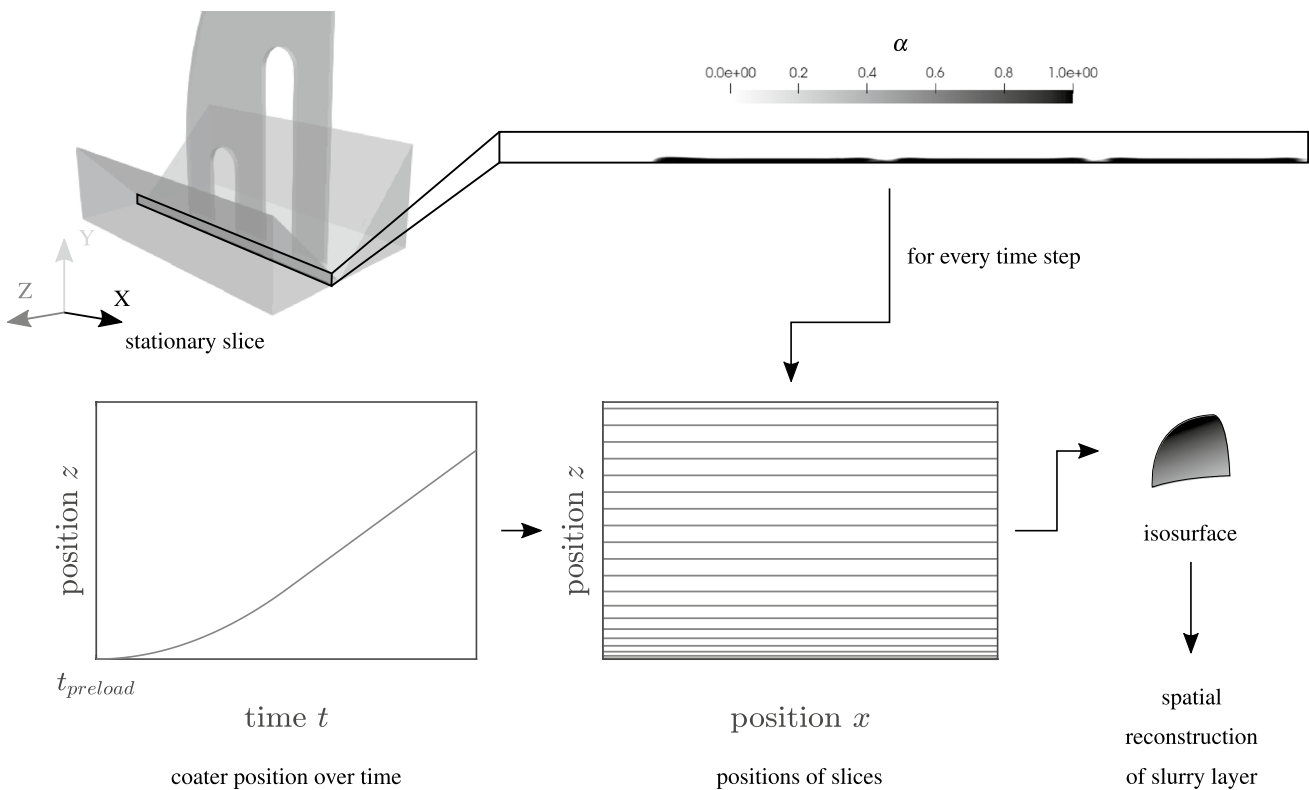

Fig. 7 Exemplary reconstruction of the slurry layer based on temporal data. The coating velocity increases linearly and subsequently remains constant

mesh, but far enough away from the trailing edge of the coating head so as not to be influenced by the downstream meniscus (Fig. 6). The volume fraction α of each cell within this plane is evaluated for each timestep. The result is a momentary grayscale snapshot for all timesteps of the simulation, where a white pixel indicates $\alpha = 0$ and a black pixel indicates $\alpha = 1$. Here, α is referred to as the volume fraction of a cell filled with the liquid slurry phase. These snapshots are subsequently saved in a video file. Since the substrate velocity, and therefore also the substrate position, is known for every timestep, and assuming that no slip occurs between the slurry and the substrate, the position of every snapshot can be calculated. Reverting the grayscale snapshot to the corresponding α values and incorporating the positional information leads to a three-dimensional dataset containing the α values for the reconstructed slurry layer. Calculating an isosurface on which α is equal at every point leads to the final spatial reconstruction of the slurry layer.

The spatial reconstruction was used to evaluate the surface quality of the slurry layer. The evaluation region has been restricted to the top side of the layer, a coating width of $x < 18$ mm and a coating length of $z < -20$ mm. The influence of the substrate, slurry accumulations and the outer lip is ignored here. The resulting surface data is averaged using the mean along the coating direction z to generate a two-dimensional graph. Ra is calculated from the resulting graph as the average of the surface heights in the evaluated area.

4 Simulation results

An exemplary simulation set is used to confirm an accurate implementation and representation of the model. Figure 8 shows the isosurface and stream lines at $t = 2.25$ s. The isosurface for $\alpha = 0.5$ as well as the stream lines that start in the three distribution channels coloured according to the velocity magnitude $|\mathbf{u}|$ are shown. As can be seen, the preloading process results in an upstream meniscus in front of the coating head. The simulated average flow rate at the coating head inlet after the preloading process is $Q_{in} = 98$ mm$^3 \cdot$ s^{-1} for one half of the coating head (symmetry is used). Experimental measurements of the flow rate showed (halved) values of 102 to 113 mm$^3 \cdot$ s^{-1}, corresponding to deviations in the bandwith of 4–15 %. Taking into account the pressure gauge used in this study (reading accuracy at a scale spacing of 0.05 bar, precision category 2.5), the simulation results are considered to fit the experimental values well.

If one considers the stream lines, it becomes obvious that only particles brought out close to the coating gap are instantly deposited in the slurry layer. Particles brought out further away from the coating gap start circulating in the upstream meniscus. They leave this recirculation state once they come closer to the underlying substrate and are subsequently deposited with the substrate velocity u. A particle's trajectory in the upstream meniscus can be described as a spiral. The circular movement is superimposed by a movement away from the symmetry plane of the coating head. This is the result of the transverse slurry distribution by the waterfall coater geometry. The movement of the particles in the x-direction is in line with expectations. It becomes obvious that the waterfall coater geometry, with its channels acting like individual nozzles, inhibits consistent conditions for the settlement of each particle.

Even though the slurry was treated as one phase in the simulations, it can be assumed that not only the time available for each particle to settle varies depending on the location of the outlet, but the mentioned spiral movement is also affected by the individual size and shape of each particle. This is expected of potentially causing inhomogenities in the packing density. A superposition of capillary forces, that are crucial for particle placement in S-3DP, and transverse forces caused by recirculation in particular may lead to lower densities of the later compacted powder bed. These aspects have been taken into account when optimising the coater geometry.

Additionally, a downstream meniscus forms at the inrear of the coating head, where the slurry is sucked up. The recirculation, and therefore the increase of slurry viscosity due to contact with the water-absorbing previous layers, is assumed to further influence the layer properties. However, the aspect of potential local increase in viscosity due to water loss has not yet been studied but is recommended for further investigations.

Figure 9 shows the spatial reconstruction of the slurry layer for an exemplary simulation at $\alpha = 0.5$. As can be seen, the slurry layer shows a rugged top and bottom interface. Besides, the slurry layer exhibits several minor holes. This effect can be attributed to the simulation setup that - in contrast to the real setup - models slurry casting on an impermeable surface. This leads to a partial air entrainment at the flow front of the upstream meniscus, and to α values smaller than 1. These entrainments accumulate in front of the coating gap leading to holes in the final slurry layer. Nevertheless, this effect is ignored when evaluating the slurry layer width (outline) based on the spatial reconstructions. This is
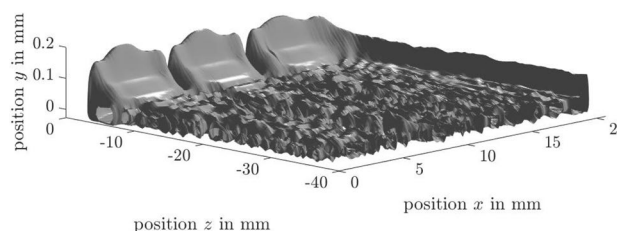

Fig. 9 Spatial reconstruction for the waterfall coating head geometry for simulation No. 1 at $\alpha = 0.5$

justified as the fluid flow creates an outer lip that is higher than the center region of the slurry layer and is hardly influenced by this effect (boundary effect). In the real system, a slurry layer is cast on a permeable substrate from layer No. 2 as multiple slurry layers are coated prior to the current one. In contrast to the simulations conducted on an impermeable surface, the capillary forces acting on the carrier liquid lead to a micro-fluid flow into the underlying layers in the real setup.

5 Validation

5.1 Approach to validation

The automated test bench used for the experiments has two axes, one in the coating direction and one for lifting and lowering the building platform. The moving unit in the coating direction includes the coater, connected to a slurry reservoir via a tubing section, a print head connected to a reservoir of binder and an IR lamp (IRD S230, Optron GmbH, Garbsen, Germany) to dry the cast layers. The coating unit is shown in Fig. 10. The operating time of the IR lamp is controlled for each individual layer by a stationary infrared sensor (CT-SF-22, Micro-Epsilon Messtechnik GmbH & Co. KG, Ortenburg, Germany) to ensure homogeneous drying. The slurry flow is toggled by a directional valve that applies a pre-set pressure on the slurry reservoir. The motion of the axes, the directional control valve and the drying unit are controlled by a programmable logic controller (PLC) based on SIMATIC S7 (Siemens Aktiengesellschaft, Munich, Germany). A stationary cleaning unit acts as a cleansing and moisture retention system for the coater during drying.

Coating simulations and spatial reconstructions are carried out for five different parameter sets to address varying

coating velocities u and gap heights h_g. Zocca et al. [29] suggest selecting a deposition speed of $50 \, mm \cdot s^{-1}$ for silicate ceramic slurries and $100 \, mm \cdot s^{-1}$ for technical ceramics. In this paper, coating velocities u are chosen at values between 50 and $97.5 \, mm \cdot s^{-1}$ according to Table 4. The velocities for a layer height of $h_g = 0.1 \, mm$ (specimen 1–4) are adjusted to four discrete values. The coating velocity of specimen 5, with layers of $0.075 \, mm$ height, is scaled up to $97.5 \, mm \cdot s^{-1}$. This setting corresponds to medium amounts of deposited slurry according to the reduced layer height.

The experiments are performed to compare simulation results with visually recognisable effects and measured values. Table 5 shows the process parameters that are kept constant in this study. The pressure set at the pressure reducing valve $p_{slurry} = 0.95 \, bar$ and the preloading time $t_{preload} = 1.5 \, s$ are equal for all specimens. The final substrate velocity u in the simulations corresponds to the respective velocity of the coater in the experiments and is reached within $0.5 \, s$ after the preloading step. The aqueous quartz slurry Q24 used contains 44 vol-% solid quartz particles with a mean diameter of $<5 \, \mu m$. A temperature-controlled drying setup has been preferred over time-controlled drying for this study as previous experiments showed a more homogeneous layer quality with this method. However, measuring absolute temperatures on the surface of a freshly cast layer with a pyrometer is very challenging as the emission coefficient depends on the moisture content of the layer and therefore changes over time. Furthermore, the infrared sensor reacts very sensitively to the radiation of the IR lamp that is applied during measurement in the present setup. Quantifying the absolute temperature of the layers is not part of this paper. Neither the
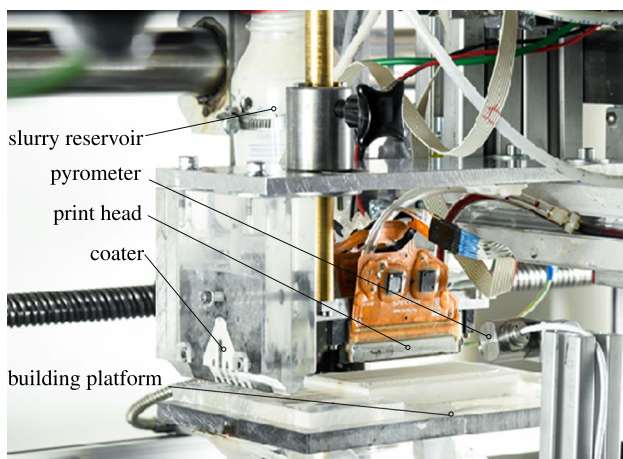

Fig. 10 Coating unit

Table 4 Parameters varied in the experiments, simulations and spatial reconstructions

Specimen/ simulation No.	u in $mm \cdot s^{-1}$	h_g in mm
1	55	0.1
2	65	0.1
3	80	0.1
4	95	0.1
5	97.5	0.075

Table 5 Constants in setup and process

Constant	Value	Unit
Substrate material	Plexiglass, sandblasted	
Slurry material	Quartz slurry Q24	
Pressure	0.95	bar
Preload time	1.5	s
Target layer temperature	55.0	°C
Building height of specimen	4.0	mm

IR lamp nor the pyrometer setup has been changed in this study, so the drying conditions are assumed to be constant for every specimen.

Dimensioned photographs are used to compare the simulation and the experimental results. Images of the experimentally produced specimens were perspectively corrected by calibrating the images using the fixed rectangular dimension of the substrate block. The specimen images as well as the reconstructed outlines are saved as new image files with a resolution of $1 \times 10^{-4} \frac{mm}{px}$ and graphically superimposed. Roughness measurements on a MarSurf M 400 surface measuring instrument (Mahr GmbH, Göttingen, Germany) using the probe arm BFW A 10-45-2/90° allow further detailed investigations.

5.2 Validation results

5.2.1 Evaluation of the outlines

The overlay of the respective outlines of the spatial reconstructions and the dimensioned photographs of the specimens are shown in Figure 11. The first layer of each specimen was cast at velocities $\ll u$ to balance inaccuracies in the adjustment of the gap between the coater and the plane of the substrate. One layer of slurry of a higher, unevaluated width is thus visible below the actual specimen.

The reconstructed slurry layers are of different lengths as the simulated times are all set equally to $t_s = 2.5$ s while u is different. As can be seen, the outline of a single slurry layer agrees well with the specimens for varying substrate velocities u and for varying gap heights h_g. Both the slurry

accumulations at the beginning of the coating process and the overall width of the slurry layer can be predicted well. This accordance with different parameter settings (based on relevant settings and proportions for S-3DP) indicates the suitability of the presented simulation methods.

One difference that is present in all specimens is the abrupt increase in width at the beginning of the slurry layer. The transition that occurs in the simulations is more continuous. This can be attributed to the non-constant acceleration of the coating machine. To reduce mechanical loads, it uses a linear increase and decrease in acceleration on reaching the final substrate velocity, which may lead to the apparent deviations.

5.2.2 Evaluation of the surface roughness

The spatial reconstruction was also used to evaluate the surface quality of the slurry layer. To this end, only the top side of the slurry layer was examined by restricting the evaluation to the vertices positioned along the vertical (y) direction more than half the gap height $\frac{h_g}{2}$ away from the substrate. The resulting data is shown for simulation No. 1 and $\alpha = 0.5$ in Fig. 12 together with a single surface measurement for the corresponding specimen. As three measurements of Ra at varying positions along the coating direction showed a standard deviation of only 0.044 μm, the experimentally determined surface profile is considered being representative for the respective specimen. However, an analysis of an increased number of specimens is recommended in future investigations to achieve statistical power. The position of the surface measurement cannot be determined precisely due to the test apparatus but is expected to roughly match the
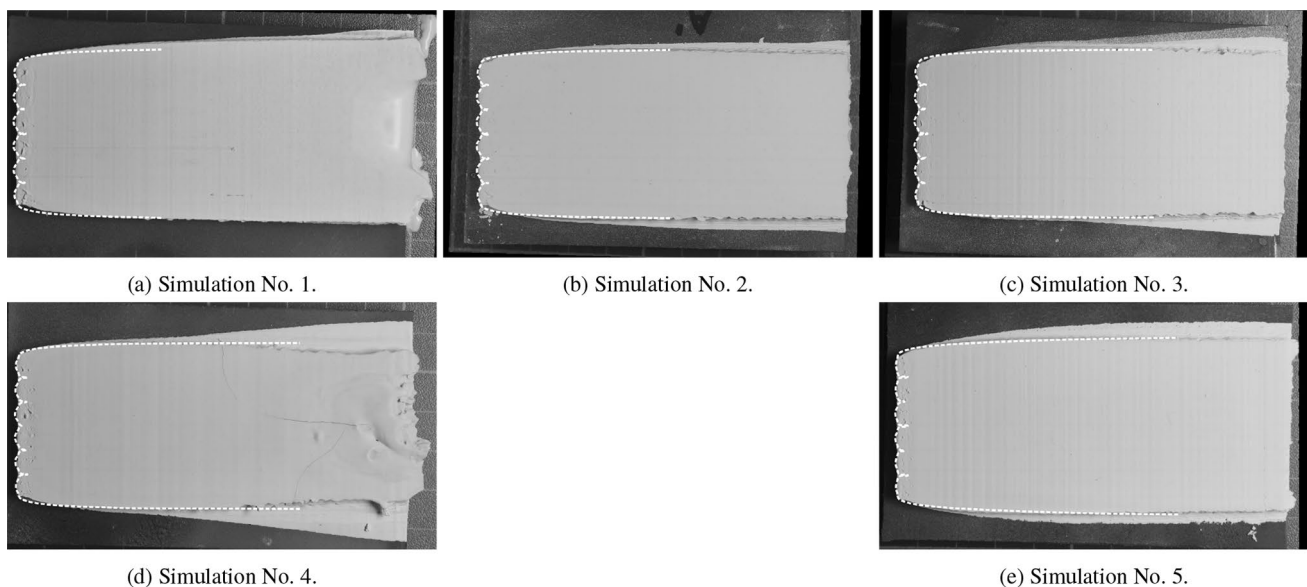

(a) Simulation No. 1.   (b) Simulation No. 2.   (c) Simulation No. 3.

(d) Simulation No. 4.   (e) Simulation No. 5.

Fig. 11 Overlay of the outline of the spatial reconstructions and the perspective-corrected images of the physically produced specimens
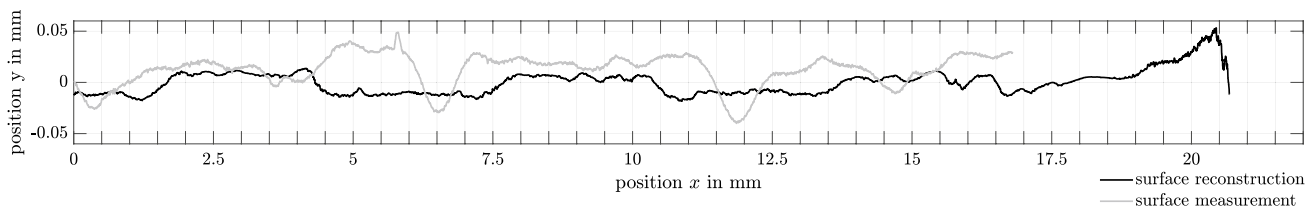
Fig. 12 Surface reconstruction for $\alpha = 0.5$ and surface measurement for the corresponding specimen

positions of the surface reconstruction. Position $x = 0\,\text{mm}$ equals the symmetry plane of the coater for the values determined by simulation. The first coater channel stretches from position $x = 1.5\,\text{mm}$ to $x = 4.5\,\text{mm}$, the second from $x = 7.5\,\text{mm}$ to $x = 10.5\,\text{mm}$ and the third from $x = 13.5\,\text{mm}$ to $x = 16.5\,\text{mm}$.

As can be seen, both the reconstruction and the specimen show valley and plateau regions. This effect is caused by the distribution channels of the waterfall coating head geometry. More slurry is deposited directly behind a channel compared to the inter-channel regions. Additionally, grooves along the coating direction are formed in the experiments and can also be seen in the reconstruction. However, the surface of the specimen was formed to its final shape by multiple layers one on top of the other. This may cause averaging, blurring and overlay effects. Nevertheless, it can be said that the simulation shows roughness values of the same magnitude as the experimental measurements.

As already mentioned, air entrainment occurs in the simulation due to the impermeable substrate. The averaging process along the coating direction minimises its influence on the results. As soon as the number of defects in the slurry layer generated by the simulation increases, the reconstruction of the averaged surface becomes increasingly distorted. This amount depends on the α value chosen when constructing the isosurface.

Until now, the most commonly used value of $\alpha = 0.5$ has been used for this process. This ensures that the assignment of a cell center to either side of the slurry-air interface is judged by whether more than half the cell is filled with slurry. Altering this value to $\alpha = 0.25$ reduces the influence of the air entrainment as additional cells are then assigned to the slurry side of the slurry-air interface. Nevertheless, this approach has to be applied with care as choosing values that are too low will lead to a loss in significance of the results.

The surface roughness of the produced layers directly affects the feasible roughness of a 3D-printed part as well as the feasible roughness of the metal casting. This makes it one of the crucial properties for 3D-printed moulds and cores. To allow a comparison with the specimens, the average roughness Ra is evaluated in both cases. Whereas the surface reconstruction already forms a characteristic representation of the entire slurry layer, the representativity of the

Ra values for the physical specimens is ensured by determining the Ra value along three different planes perpendicular to the coating direction and subsequently calculating the mean of these three values.

The results for the simulations using an isosurface for $\alpha = 0.5$ and $\alpha = 0.25$ as well as for the specimens depending on the substrate velocity u for $h_g = 0.1\,\text{mm}$ are shown in Fig. 13. The simulated and experimental results are in the same regime for both α values. The experimental results indicate that the average roughness Ra increases with increasing substrate velocities u, and thus the surface quality diminishes. This trend is not present in the simulation results for both α values. Ra decreases with increasing u, suggesting an inverse behaviour. If one considers $\alpha = 0.25$, a good approximation for $u < 65\,\text{mm}\cdot\text{s}^{-1}$ is apparent. The influence of the air entrainment becomes too large at higher substrate velocities, leading to distorted Ra values. For $\alpha = 0.5$, this influence seems to be present in the entire investigated velocity regime and prohibits a prediction that is more precise than the magnitude of Ra. As Fig. 13 reveals substantial discrepancies between the experimental and the simulation results of Ra at higher coating velocities, the deviations are presumed to be decisively influenced by the material model that defines a shear thinning flow behaviour during the entire slurry coating process leading to smoothing characteristics. In the experiments, the slurry's viscosity is presumed to rapidly increase due to the loss of water when in contact with
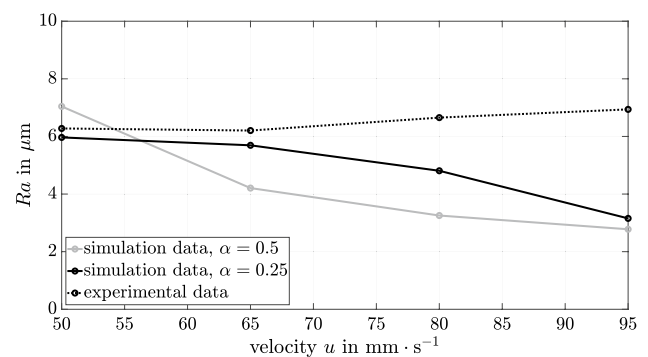

Fig. 13 Influence of the velocity on the surface roughness for the spatial reconstruction and the experiments for $h_g = 0.1\,\text{mm}$

the underlying layers. Implementing an altering viscosity behaviour shall be part of future investigations.

6 Application – optimisation of the coater geometry

Because weaknesses have been identified in the waterfall coater geometry, the methods described above are carried out iteratively for multiple alternative coating head geometries with the aim of increasing the coating process quality. Subordinate objectives of the optimisation should lower the hurdles for an industrial implementation and scale-up of the additive manufacturing process in advance:

– minimise surface roughness
– reduce cycle times
– minimise regions of low velocities (to avoid deposits of hardened slurry and improve cleanability)
– generate a uniform velocity distribution at the outlet (to increase homogeneity)
– avoid movements of particles perpendicular to the casting direction (to avoid transverse forces on the slurry)
– provide slurry on demand (to reduce excess material and simplify homogeneous drying)

The optimisation iteration process began with a coat hanger design that is usually employed in the polymer production of films and sheets [3, 6]. A known design was adapted to the required dimensions and boundary conditions. Three major iteration steps with multiple sub-iterations were carried out manually to optimise the design. Those major steps were a single-step coat hanger design with sharp cavity edges, a single-step coat hanger design with rounded cavity edges and the final two-step coat hanger design with rounded cavity edges. The main alignments during the iteration of geometry concerned the distribution chamber at the inlet, as it is crucial to mimimise regions of low velocities for a stable and cleanable coating device. The final geometry is depicted in Fig. 14.

The simulative methods introduced here were used to determine a suitable parameter set for the optimised coat hanger design. The optimal substrate velocity was discovered to be $u = 65 \text{ mm} \cdot \text{s}^{-1}$. The corresponding pressure p_{slurry} is 1.398×10^5 Pa for a filling height of $h_r = 70$ mm. The preloading step was eliminated as there is no need to connect the single beads of the channels to build up a slurry front and the new design allows for instant coating on a moving substrate. The cycle time can not only be reduced by the eliminated preloading time itself, but also because there is no need for acceleration and deceleration when entering the building area. The design for a slurry-on-demand deposition implies no relevant recirculation of slurry in front of
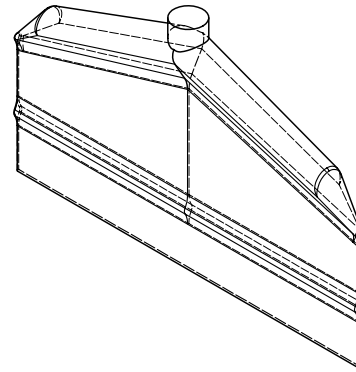

Fig. 14 Final, optimised geometry based on a coat hanger design. The inner cavity is depicted
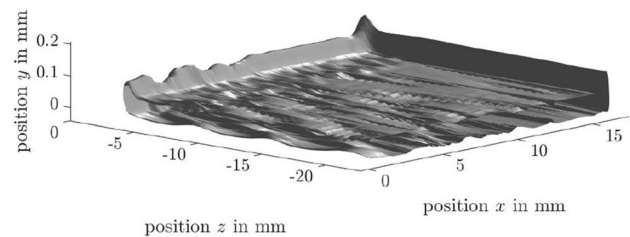

Fig. 15 Spatial reconstruction for the optimised coating head geometry for $u = 65 \text{ mm} \cdot \text{s}^{-1}$ at $\alpha = 0.5$

the coater and a minimised amount of excess material. The spatial reconstruction of this simulation for $\alpha = 0.5$ is shown in Fig. 15 . As can be seen, there is no air entrainment to distort the slurry-air interface. Additionally, slurry deposition at the beginning of the coating process is more homogeneous over the entire coating gap width. The accumulations at the beginning are due to the slurry forming droplets at the coating head outlet. The interface touches the moving substrate at slightly varying times leading to this effect. However, it is of minor influence.

In contrast to the waterfall coater geometry, the optimised geometry produces a slurry layer of a constant width during the entire coating process. This leads to an excellent scalability of the process on a coating area extended in the coating direction. However, an assembly of multiple, in-line coating units becomes technically challenging. For a scale up of the coat hanger geometry capable of applying slurry over an extended coating width, it is suggested that the geometry be redesigned using the optimised geometry as a basis and iterative simulations as described above. Compared to an exemplary reconstruction for the waterfall coater as shown in Fig. 9, the increased surface quality becomes obvious. There are no visible plateaus, valleys or grooves like those attributable to the channel structures of the waterfall coater geometry. The superior surface quality is supported by a

decreased averaged roughness $Ra = 0.79\,\mu$m. An uncertainty in practice regarding this value is expected to persist due to the fact that in reality a suspension comprising of a fluid phase and particles is processed instead of a homogeneous liquid solution. The resulting surface quality is thus expected to be further influenced by particle settling and drying dynamics that were disregarded within the simulation methods described herein. Furthermore, as discussed in 5.5.2, an enhanced material model integrating an altered viscosity behaviour when in contact with permeable surfaces is needed to allow a realistic prediction of the Ra values. However, the optimised geometry is expected to be capable of producing smooth surfaces with an improved homogeneity for the entire coating area.

7 Conclusion

This article proposed a CFD approach to simulate the slurry casting process as a crucial step for S-3DP. A method has been introduced for the spatial reconstruction of layers with little computational effort. It could be demonstrated that this simulation approach is a useful tool to indicate the macroscopic behaviour and defects within each layer and propose geometries and process parameter settings for an optimisation that requires few experiments. The proposed surface reconstruction method allows an approximation of the magnitude of the resulting surface roughness. Achieving uniform macroscopic layer properties is expected to have a major impact on both homogeneous drying conditions within each layer (and therefore the resulting microscopic powder bed characteristics) and the scalability of the process from lab-scale to an industrial setup. However, this study is rated as an initial validation approach for the suggested methods to simulate the casting of slurry layers in S-3DP. The slurry itself was initially simulated as one phase without taking into account the ongoing fluid evaporation and the fluid flow through the underlaying layers. Future investigations are necessary so that the simulation can include a dynamic flow behaviour of the slurry due to the permeability of previously cast layers. This means that the evidence on the resulting properties of the cast layers still needs to be improved by solving the issue of viscosity modification within the casting process in the simulation and providing statistical data in the experimentation in parallel. Furthermore, a computational reproduction of multiple layers will be of interest for a simulation of the S-3DP process as well as experimental proof of the optimised coat hanger design.

Declarations

References

1. AlMangour B (2018) Additive manufacturing of emerging materials. Springer, Cham,. https://doi.org/10.1007/978-3-319-91713-9
2. Brackbill JU, Kothe DB, Zemach C (1992) A continuum method for modeling surface tension. J Comput Phys 100(2):335–354. https://doi.org/10.1016/0021-9991(92)90240-y
3. Carneiro O, Nobrega JM (2012) Design of Extrusion Forming Tools. iSmithers Rapra Publishing, Shrewsbury
4. Chantaramee N, Tanaka S, Takahashi T, Uematsu K (2008) Evolution of discontinuity in particle orientation in ceramic tape casting. J Am Ceramic Soc 91(10):3181–3184. https://doi.org/10.1111/j.1551-2916.2008.02605.x
5. Günther D, Mögele F (2016) Additive manufacturing of casting tools using powder-binder- jetting technology. In: Shishkovsky IV (ed) New Trends in 3D Printing, InTech, 10.5772/62532
6. Han W, Wang X (2012) Optimal geometry design of the coat-hanger die with uniform outlet velocity and minimal residence time. J Appl Polymer Sci 123(4):2511–2516. https://doi.org/10.1002/app.34827
7. Jabbari M, Bulatova R, Hattel JH, Bahl C (2014) An evaluation of interface capturing methods in a vof based model for multiphase flow of a non-newtonian ceramic in tape casting. Appl Math Model 38(13):3222–3232. https://doi.org/10.1016/j.apm.2013.11.046
8. Kistler SF, Schweizer PM (2012) Liquid film coating: scientific principles and their technological implications. Springer, Netherlands, Dordrecht
9. Lin YY, Wu PY, Liu TJ, Hsu TC, Tiu C (2013) Coating die design for suspensions. Asia-Pac J Chem Eng 8(1):115–129. https://doi.org/10.1002/apj.1636
10. Loest H, Lipp R, Mitsoulis E (1994) Numerical flow simulation of viscoplastic slurries and design criteria for a tape casting unit. J Am Ceramic Soc 77(1):254–262. https://doi.org/10.1111/j.1151-2916.1994.tb06986.x
11. Mostafaei A, Elliott AM, Barnes JE, Li F, Tan W, Cramer CL, Nandwana P, Chmielus M (2020) Binder jet 3d printing–process parameters, materials, properties, modeling, and challenges. Progress Materials Sci 40(1160):100707. https://doi.org/10.1016/j.pmatsci.2020.100707

12. Mühler T, Gomes CM, Heinrich J, Günster J (2015) Slurry-based additive manufacturing of ceramics. Int J Appl Ceramic Technol 12(1):18–25. https://doi.org/10.1111/ijac.12113
13. Mühler T, Wirth C, Ascheri M, Nicolaides D, Heinrich J, Günster J (2015) Slurry-based powder beds for the selective laser sintering of silicate ceramics. J Ceramic Sci Technol 6(2):113–118. https://doi.org/10.4416/JCST2015-0007
14. Nagasawa Y, Uematsu M, Takahashi Y, Kato Z, Uematsu K, Tanaka S (2015) Observation of particle motion in high-concentration ceramic slurries under low shear rate. J Am Ceramic Soc 98(5):1429–1436. https://doi.org/10.1111/jace.13498
15. Nieves-Remacha MJ, Yang L, Jensen KF (2015) Openfoam computational fluid dynamic simulations of two-phase flow and mass transfer in an advanced-flow reactor. Industrial Eng Chem Res 54(26):6649–6659. https://doi.org/10.1021/acs.iecr.5b00480
16. OpenCFD Limited (2019) Openfoam programmer's guide: Version v1912
17. Sachs E (1997) High green density ceramic components fabricated by the slurry-based 3DP process. University of Texas at Austin, 10.15781/T2DV1D80B
18. Sachs EM, Haggerty JS, Cima MJ, Williams PA (1993) Three-dimensional printing techniques
19. Sachs EM, Cima MJ, Caradonna MA, Grau J, Serdy JG, Saxton PC, Uhland SA, Moon J (2000) Jetting layers of powder and the formation of fine powder beds thereby
20. Seidel A (30.11.2020) Numerical simulation and optimisation of the slurry-based layer casting process in additive manufacturing of ceramic parts. Master's thesis, Technical University of Munich, Munich
21. Simón Muzás J (01.04.2020) Production and characterization of ceramic layer compounds: Experimental design and optimization process. Master's thesis, Technical University of Munich, Munich
22. Tian X, Li D, Heinrich JG (2012) Rapid prototyping of porcelain products by layer-wise slurry deposition (lsd) and direct laser sintering. Investigation Fluid Flow During Recoating Process Additive Manuf 18(5):362–373. https://doi.org/10.1108/13552541211250364
23. Travitzky N, Bonet A, Dermeik B, Fey T, Filbert-Demut I, Schlier L, Schlordt T, Greil P (2014) Additive manufacturing of ceramic-based materials. Adv Eng Materials 16(6):729–754. https://doi.org/10.1002/adem.201400097
24. Upadhyay M, Sivarupan T, El Mansori M (2017) 3d printing for rapid sand casting–a review. J Manuf Process 29(6):211–220. https://doi.org/10.1016/j.jmapro.2017.07.017
25. Vogt J, Stepanyan M, Erhard P, Günther D, Schmalzl S, Gläser S (2021) Slurry-based additive manufacturing of casting cores: A cross between material-, process- and device development. InCeight Casting C8:1
26. Wagner W, Kretzschmar HJ, Span R, Krauss R (2010) D2 properties of selected important pure substances. In: VDI Heat Atlas, Springer Berlin Heidelberg, Berlin, Heidelberg, pp 153–300, 10.1007/978-3-540-77877-6_11
27. Wonisch A, Polfer P, Kraft T, al e (2011) A comprehensive simulation scheme for tape casting: From flow behavior to anisotropy development. Journal of the American Ceramic Society 94(Nr.7):2053–2060
28. Yen HC (2015) Experimental studying on development of slurry-layer casting system for additive manufacturing of ceramics. Int J Adv Manuf Technol 77(5–8):915–925. https://doi.org/10.1007/s00170-014-6534-8
29. Zocca A, Colombo P, Gomes CM, Günster J (2015) Additive manufacturing of ceramics: Issues, potentialities, and opportunities. J Am Ceramic Soc 98(7):1983–2001. https://doi.org/10.1111/jace.13700
30. Zocca A, Lima P, Günster J (2017) Lsd-based 3d printing of alumina ceramics. Journal of ceramic science and technology 8(1, SI):141–147, 10.4416/JCST2016-00103